ChemComm

COMMUNICATION

View Article Online
View Journal | View Issue

Cite this: *Chem. Commun.*, 2025, **61**, 11826

Received 1st June 2025,
Accepted 30th June 2025

DOI: 10.1039/d5cc03109e

rsc.li/chemcomm

Nano-silicon/reduced graphene oxide composite anodes for high performance all solid-state batteries†

Ayush Morchhale,‡[a] Dawoon Jang,‡[a] Jun Wei Yap,[a] Lakshmi Surag Singavarapu,[b] Sadikul Alam,[b] Jinwoo Hwang,[b] Sungjin Park [c] and Jung-Hyun Kim *[a]

Nano-Si (n-Si) encapsulated with SiO_x shells and anchored onto reduced graphene oxide (rGO) *via* hydrothermal self-assembly is demonstrated as a promising solid-state battery anode. Compared to simple n-Si, this composite anode exhibited improved rate capability and cycle life, enabled by robust Si–O–C bonding, mechanical reinforcement, and rapid electron transport.

Sulfide-based all solid-state batteries (SSBs) have emerged as prominent next-generation energy storage devices due to their potential for enhanced safety and energy density compared to conventional lithium-ion batteries.[1,2] Despite significant progress, sulfide-based SSBs still face critical challenges at the anode/solid electrolyte (SE) interface, especially when using Si anodes.[3] While Si offers high theoretical capacity (4200 mAh g^{-1} for $Li_{4.4}Si$) compared to traditional graphite anodes (372 mAh g^{-1}), its practical application has been hindered by electro-chemo-mechanical instabilities.[4] Large volume expansions (>300%) of the Si anode during cycling induce severe mechanical stresses at the anode/SE interface, leading to rapid capacity fading, SE cracking, and premature cell failure.[5] Resolving this interfacial instability is critical, as the adoption of Si anodes for SSBs enables substantial improvements in energy density, driving range, fast-charging capability, and overall safety, which are key factors for the widespread adoption of electric vehicles (EVs).

Addressing the electro-chemo-mechanical instability of Si in SSBs remains challenging due to the complex interactions at the nanoscale interfaces, a limited understanding of the underlying degradation mechanisms, and the lack of effective *in situ* characterization tools.[6] The most common approach has been replacing micron-sized Si particles with nano-sized Si (n-Si) particles, which can alleviate stress accumulation and mitigate subsequent mechanical degradation.[7] However, the current approach to stabilize n-Si in sulfide-based SSBs remains insufficient. A major issue lies in the intrinsically low electronic conductivity and limited Li^+ diffusivity of n-Si based anodes, which further exacerbate their electro-chemo-mechanical instability.

To solve the Si/SE interfacial problems, we introduced n-Si particles coated with a conformal SiO_x shell, which are chemically anchored onto reduced graphene oxide (rGO) nanoplatelets. While the enhanced performance of this chemically modified anode (hereafter referred to as n-Si/G) has been demonstrated in Li-ion batteries,[8–10] its impact in sulfide-based SSBs has yet to be fully explored. In this work, n-Si/G powder samples were prepared *via* one-pot hydrothermal reaction. The SiO_x shell offers moderate Li-ion conductivity (~1 μS cm^{-1})[11] due to its amorphous structure and serves as a chemically and mechanically stable interfacial layer that mitigates direct contact between the Si core and the argyrodite-type $Li_6PS_5Cl_{0.5}Br_{0.5}$ SE.[10,12] The covalent Si–O–C bonding between the Si@SiO_x nanoparticles and rGO nanoplatelets ensures strong interfacial adhesion, enhancing structural integrity and effectively accommodating volumetric changes during cycling.[13]

Fig. 1a displays the uniform dispersion of n-Si particles onto the rGO supports, as observed by scanning electron microscopy (SEM). Its transmission electron microscopy (TEM) image (Fig. 1b) reveals an ~ 3 nm thick SiO_x shell surrounding the n-Si particles. High-angle annular dark field scanning transmission electron microscopy (HAADF-STEM) images (Fig. 1c and 1d) reveal n-Si particles, with diameters ranging from 30 to 50 nm, anchored on the rGO layers. Fig. 1c and e–g show energy-dispersive X-ray spectroscopy (EDS) mapping images displaying the elemental distribution of Si, C, and O on the surface of the n-Si/G particles. The SiO_x nanoparticles are uniformly distributed on the rGO layers.

X-ray photoelectron spectroscopy (XPS) was performed to analyze the chemical states of the n-Si/G composite. As shown in Fig. 1h, the deconvoluted C 1s spectrum of the n-Si/G

[a] *Department of Mechanical and Aerospace Engineering, The Ohio State University, Columbus, Ohio 43210, USA. E-mail: kim.6776@osu.edu*
[b] *Department of Materials Science and Engineering, The Ohio State University, Columbus, Ohio 43210, USA*
[c] *Department of Chemistry and Chemical Engineering, Inha University, 100 Inha-ro, Michuhol-gu, Incheon 22212, Republic of Korea*

† Electronic supplementary information (ESI) available. See DOI: https://doi.org/10.1039/d5cc03109e

‡ These authors contributed equally.

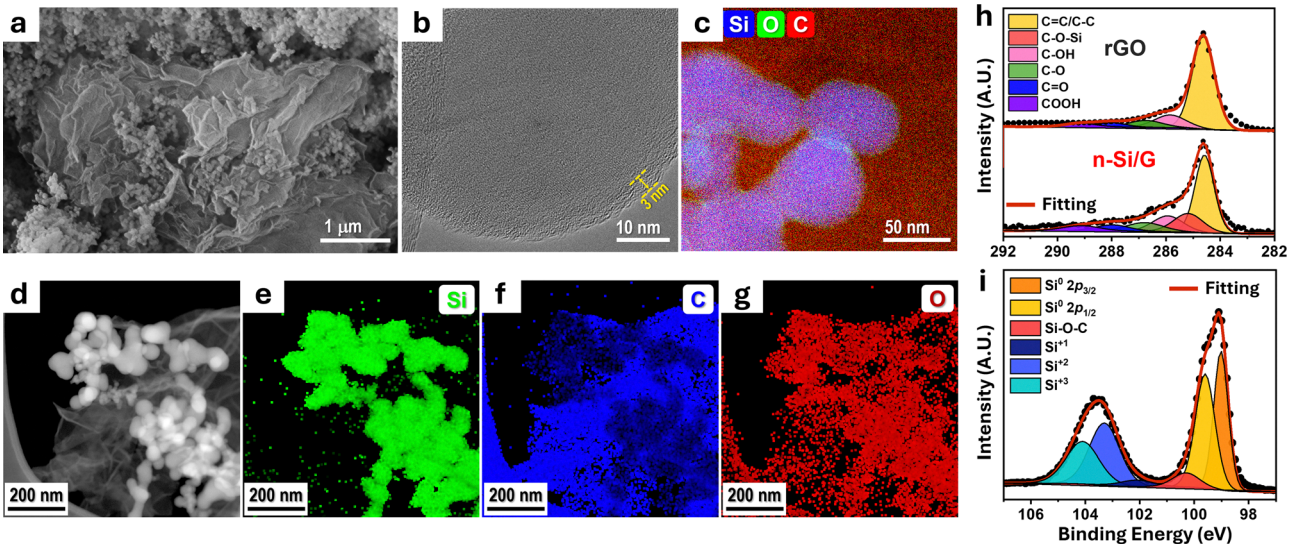

Fig. 1 (a) SEM, (b) TEM, and (c)–(g) STEM-EDS images of the n-Si/G samples. The TEM image focused on a single n-Si particle within the n-Si/G. (h) C 1s XPS spectra of the rGO and n-Si/G sample. (i) Si 2p XPS spectra of the n-Si/G sample (circular dots: experimental data, solid lines: fitting curves).

composite exhibits six peaks at 284.6, 285.2, 285.9, 286.7, 288.0 and 289.1 eV, corresponding to C═C/C–C, C–O–Si, C–OH, C–O, C═O, and COOH bonds, respectively (Fig. 1h). The peak at 285.2 eV is attributed to the new formation of Si–O–C bonds arising from the chemical bonding between the SiO_x and rGO layers. Meanwhile, the intensity of the C═C/C–C peak, originating from the rGO, decreased as a result of bonding with SiO_x in the n-Si/G sample. In the deconvoluted Si 2p spectrum of the n-Si/G composite (Fig. 1i), distinct peaks were observed corresponding to metallic silicon: Si $2p_{3/2}$ at 99.0 eV and Si $2p_{1/2}$ at 99.6 eV. In addition, a peak at 100.3 eV is attributed to Si–O–C bonding, whereas peaks at 102.0, 103.3, and 104.0 eV correspond to oxidized Si species with oxidation states of Si^{+1}, Si^{+2}, and Si^{+3}, respectively, further confirming the presence of the SiO_x outer shell. This result is consistent with the TEM data (Fig. 1b and c), which showed SiO_x shells surrounding the n-Si particles, while metallic Si remains predominantly confined to the particle cores.

The electrochemical performance of the n-Si/G anodes was evaluated using SSB full-cells. For cathodes, single-crystal $LiNi_{0.6}Mn_{0.2}Co_{0.2}O_2$ (NMC622) was coated with 1 wt% $LiNbO_3$ (LNO) to passivate the cathode/SE interface.[1] In this work, all the SSB cells were cycled under a constant stack pressure of 5 MPa. Fig. 2a presents the long-term cycle life of SSB full-cells at room temperature (RT). The full cell with the n-Si/G anode delivered an initial discharge capacity of 169 mAh g^{-1} at C/10, with a 1st cycle coulombic efficiency (CE) of 75%, compared to 172 mAh g^{-1} and 71% for the full cell with the simple n-Si anode. Between the 4th and 50th cycles at C/5, the n-Si/G anode offered improved capacity retention (93%) relative to the n-Si anode (87%). Fig. 2b and c shows the voltage profiles of the full-cells at the 1st, 5th, and 50th cycles. The simple n-Si anode showed larger voltage drops ($\Delta V = I{\cdot}\Delta R$) with cycle number, indicating greater cell-resistance growth (ΔR) compared to the n-Si/G anode. This could be due to the possible microstructural degradation of the n-Si anodes.

The impact of n-Si/G anodes on the rate capability of SSB full-cells was examined across various C-rates ranging from C/10 to 1C at RT (Fig. 2d). The full-cell with the simple n-Si anode had 169 mAh g^{-1} at C/10 (5th cycle), 144 mAh g^{-1} at C/5 (10th cycle), 122 mAh g^{-1} at C/3 (15th cycle), 99 mAh g^{-1} at C/2 (20th cycle), 67 mAh g^{-1} at 1C (25th cycle), and 151 mAh g^{-1} at C/10 (30th cycle). The cell exhibited an overall capacity retention of 86% at C/10 after 30 accelerated rate tests. In contrast, the full cell with the n-Si/G anode exhibited significantly improved rate capability, achieving an overall capacity retention of 96% at C/10 after 30 accelerated rate tests. For example, it delivered 165 mAh g^{-1} at C/10 (5th cycle), 149 mAh g^{-1} at C/5 (10th cycle), 132 mAh g^{-1} at C/3 (15th cycle), 116 mAh g^{-1} at C/2 (20th cycle), 97 mAh g^{-1} at 1C (25th cycle), and 161 mAh g^{-1} at C/10 (30th cycle). The n-Si/G anode exhibited a 44.8% increase in capacity at 1C charging compared to the n-Si anode.

To elucidate the superior rate capability and capacity retention of the n-Si/G anode relative to the simple n-Si anode, electrochemical impedance spectroscopy (EIS) combined with distribution of relaxation times (DRT) analysis was performed on the full-cells. Fig. 3a shows the Nyquist plots of SSB full-cells with simple n-Si and n-Si/G anodes, measured at 50% state-of-charge (SOC) and RT over a frequency range of 5 MHz and 50 mHz. Fig. 3b and c illustrate their corresponding DRT profiles for each cell. The resulting Nyquist plots were further processed *via* the distribution of relaxation time (DRT) technique MATLAB code developed by Wan *et al.*[14] All subsequent analyses derived from the Nyquist and DRT plots were based on interpretations established in prior studies of SSBs.[15–17] The high frequency intercept ($f > 3$ MHz) in the Nyquist plot corresponds to the bulk resistance (R_B) of the SE. The first semi-circle, corresponding to the P1 peak in the DRT profile at ~0.5 MHz is attributed to the grain boundary resistance (R_{GB}). The second large semi-circles (between 200 kHz and 1 Hz) in the Nyquist plots were deconvoluted using DRT into contributions from chemical contact resistance (R_C) for P2, and

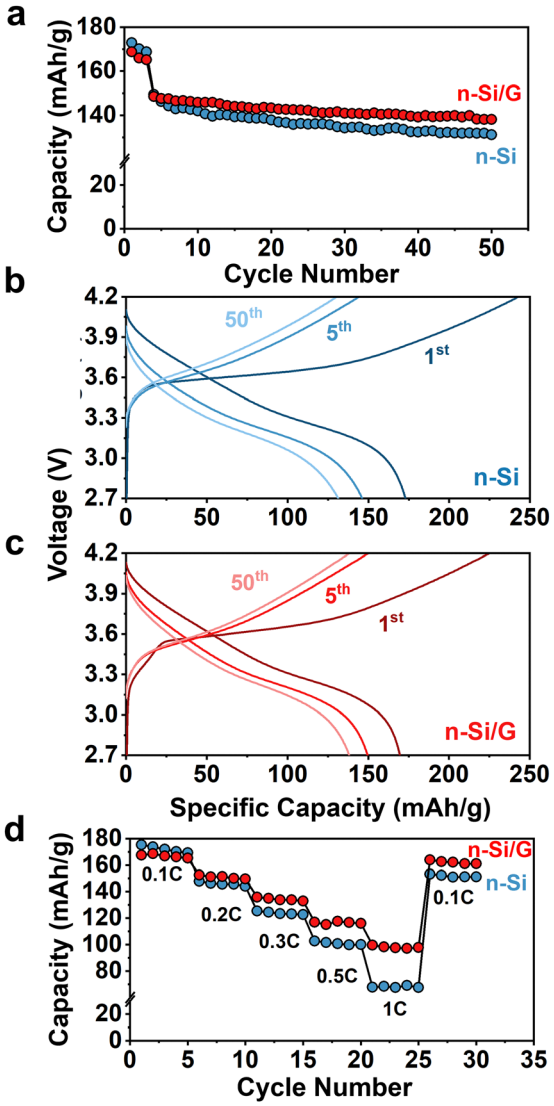

Fig. 2 (a) Cycle life and voltage profiles of (b) simple n-Si and (c) n-Si/G anodes in SSB full-cells paired with NMC622 cathodes. (d) Rate capability test of the full cells at RT, where both charging and discharging C-rates were varied from 0.1C to 1C.

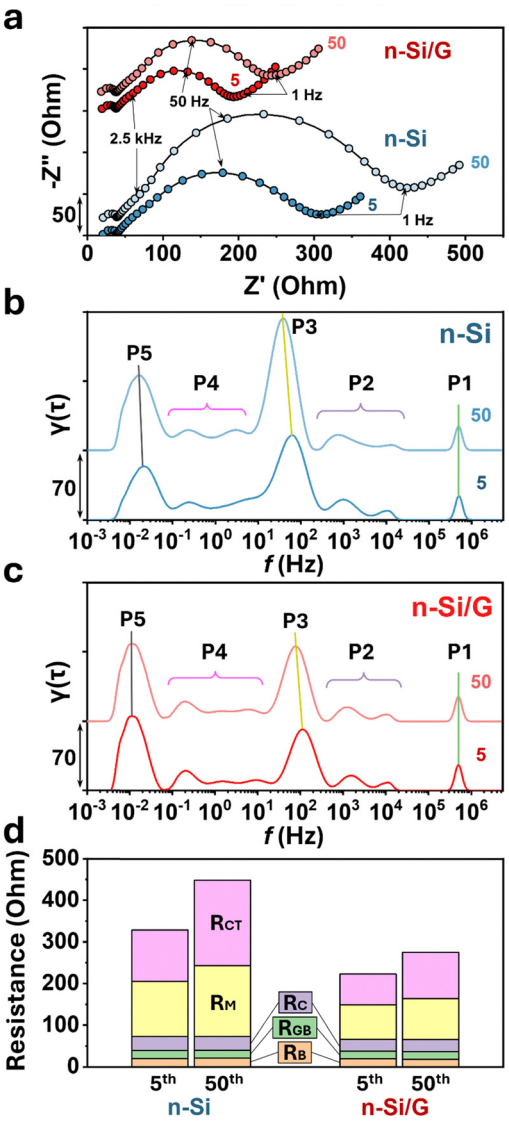

Fig. 3 (a) Nyquist plots (5th *vs.* 50th cycles) and corresponding DRT profiles of (b) simple n-Si and (c) n-Si/G anodes in SSB full-cells paired with NMC622 cathodes at 50% SOC and RT. (d) Individual contribution from different resistance sources in SSB full-cells and their evolution over 50 cycles, including bulk (R_B), grain boundary (R_{GB}), chemical contact (R_C), mechanical contact (R_M), and charge-transfer (R_{CT}) resistances.

mechanical contact resistance (R_M) for P3 at the electrode/SE interface. The P4 peak group, which arises between 25 and 0.1 Hz, corresponds to the charge transfer resistance (R_{CT}) from both the cathode and anode. Finally, the Warburg (R_W) impedances observed in the Nyquist plots at $f < 10$ mHz correspond to the P5 peaks in the DRT profiles, which is attributed to solid-state Li^+ diffusion.

Fig. 3d compares the individual contribution and evolution of resistance from different sources in the SSB full-cells over 50 cycles for the simple n-Si and n-Si/G anodes. Overall, all full-cells exhibited relatively larger R_M and R_{CT} components compared to other resistance contributions, indicating that the electrode/SE interface is the dominant source of cell resistance. After 50 cycles, the n-Si/G anode exhibited a lower total resistance increase of 24%, compared to 37% for the simple n-Si anode. Notably, the full-cell with the n-Si/G anode showed smaller increases of 18% in R_M and 52% in R_{CT}, compared to 28% in R_M and 66% in R_{CT} for the simple n-Si anode. In contrast, the R_B, R_{GB}, and R_C values remained stable over 50 cycles. It is important to note that the SSB full-cells in this work employed an ~700 μm thick SE layer, which negatively impacts the overall rate capabilities (Fig. 2d). However, the resistance contributions from the thick SE (*i.e.*, $R_B + R_{GB}$) are substantially lower than other sources (*e.g.*, R_M and R_{CT}), highlighting the superior interfacial stability between the n-Si/G anode and SE, relative to that of the simple n-Si anode.

The microstructures of the cycle-aged anodes in the SSB full-cells are shown in Fig. 4. After 50 cycles, the simple n-Si anodes exhibited large voids, up to 1 μm in size, resulting from the substantial volumetric changes of the n-Si particles. These voids degrade the contact between the n-Si and SE, leading to an increase in R_M, and subsequently hindering the charge-transfer reactions (*i.e.*,

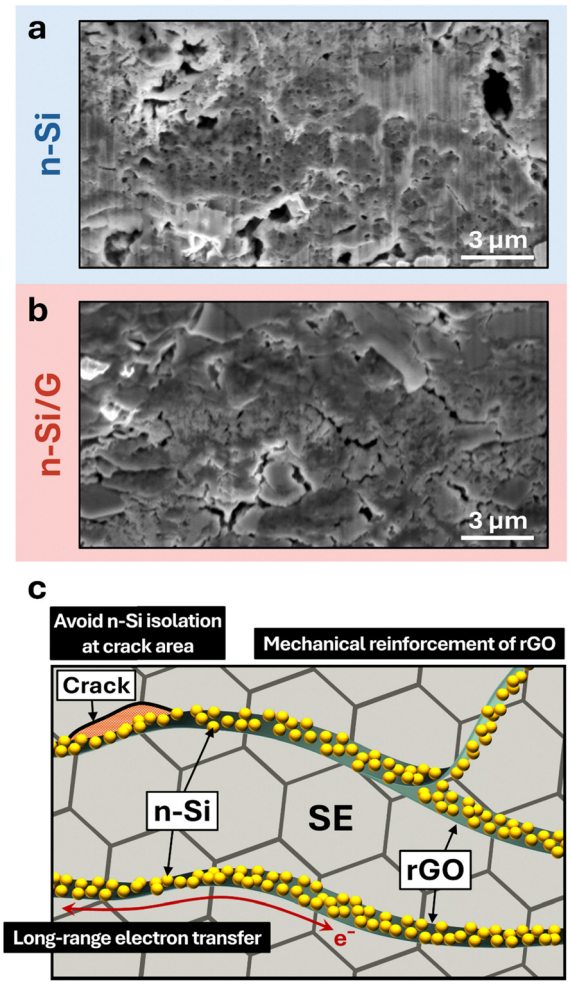

Fig. 4 FIB-SEM cross-sectional images of cycle-aged (a) simple n-Si and (b) n-Si/G anodes, recovered after 50 cycles. (c) Schematic illustration of the improvement mechanisms of n-Si/G anodes in SSB cells.

increase in R_{CT}). In stark contrast, the cycle-aged n-Si/G anode showed voids with reduced scales compared to the simple n-Si anode. rGO and graphene have been widely incorporated into various ceramic matrices to improve the mechanical properties of ceramic/rGO composites, such as fracture toughness, strength, and structural integrity.[18] In the n-Si/G composite anodes, rGO nanoplatelets serve as a flexible and robust mechanical scaffold, effectively accommodating the large volumetric changes of n-Si during cycling. This structural reinforcement suppresses interfacial degradation (*e.g.*, large pore formation), thereby preserving the mechanical integrity of the n-Si/G anodes during cycling. Moreover, even in the presence of small cracks, the extended lateral size of the rGO (>1 μm) provides a continuous electron conduction network, preventing electrical isolation of the n-Si particles anchored onto the rGO.

In conclusion, this work demonstrates that the n-Si/G composite can serve as a promising anode material for SSB full-cells. Electrochemical and microscopy analyses suggest that the enhanced rate capability and cycle life, with a capacity retention of 93%, in full-cells with n-Si/G anodes can be attributed to robust interfacial contact between n-Si and rGO through Si–O–C bonding, mechanical reinforcement of the n-Si/G + SE composite structure, and stable long-range electron transport facilitated by the rGO network. The EIS and DRT results suggest that resistance due to mechanical contact at the electrode/SE interface and charge transfer were the major components contributing towards the performance degradation. The improvement mechanism of the n-Si/G anodes is illustrated in Fig. 4c. Our results highlight the potential of n-Si/G as a promising anode material for high performance SSBs. Future research should aim to optimize the microstructure and electro-chemo-mechanical stability of the n-Si/G anodes, while also advancing scalable processing methods compatible with solid-state battery (SSB) manufacturing. In parallel, enabling stable operation under reduced external pressure could simplify cell design and lower system-level costs, thereby facilitating the broader commercialization of SSBs incorporating n-Si/G anodes.

Conflicts of interest

There are no conflicts to declare.

Data availability

The experimental methods for data collection are provided in the ESI.†

References

1 A. Morchhale, Z. Tang, C. Yu, R. Farahati and J.-H. Kim, *Curr. Opin. Electrochem.*, 2023, **39**, 101251.
2 D. H. S. Tan, Y.-T. Chen, H. Yang, W. Bao, B. Sreenarayanan, J.-M. Doux, W. Li, B. Lu, S.-Y. Ham, B. Sayahpour, J. Scharf, E. A. Wu, G. Deysher, H. E. Han, H. J. Hah, H. Jeong, J. B. Lee, Z. Chen and Y. S. Meng, *Science*, 2021, **373**, 1494–1499.
3 J. Liu, K. Pan, H. Cho, M. Canova and J.-H. Kim, *Electrochim. Acta*, 2024, **500**, 144746.
4 J. W. Yap, T. Wang, H. Cho and J.-H. Kim, *Electrochim. Acta*, 2023, **446**, 142108.
5 M. Rana, Y. Rudel, P. Heuer, E. Schlautmann, C. Rosenbach, M. Y. Ali, H. Wiggers, A. Bielefeld and W. G. Zeier, *ACS Energy Lett.*, 2023, **8**, 3196–3203.
6 J. Liu, S. Y. Lee, J. Yoo, S. Kim, J.-H. Kim and H. Cho, *ACS Mater. Lett.*, 2022, **4**, 840–846.
7 J. Kim, C. Kim, I. Jang, J. Park, J. Kim, U. Paik and T. Song, *J. Power Sources*, 2021, **510**, 230425.
8 J. K. Lee, K. B. Smith, C. M. Hayner and H. H. Kung, *Chem. Commun.*, 2010, **46**, 2025–2027.
9 M. Zhou, F. Pu, Z. Wang, T. Cai, H. Chen, H. Zhang and S. Guan, *Phys. Chem. Chem. Phys.*, 2013, **15**, 11394–11401.
10 K. Pan, F. Zou, M. Canova, Y. Zhu and J.-H. Kim, *J. Power Sources*, 2019, **413**, 20–28.
11 Z. Liu, J. Lei, W. Liu, B. Fang, L. Xie, S. Dmytro and Q. Zhang, *J. Eur. Ceram. Soc.*, 2023, **43**, 4437–4442.
12 A. Kızılaslan, Ç. G. Türk, A. Miura and K. Tadanaga, *Chem. Eng. J.*, 2024, **496**, 153588.
13 D. Zhang, P. Yu, Y. Zhang, X. Zhao and J. Yu, *ACS Appl. Energy Mater.*, 2024, **7**, 726–734.
14 T. H. Wan, M. Saccoccio, C. Chen and F. Ciucci, *Electrochim. Acta*, 2015, **184**, 483–499.
15 C.-Y. Yu, J. Choi, J. Dunham, R. Ghahremani, K. Liu, P. Lindemann, Z. Garver, D. Barchiesi, R. Farahati and J.-H. Kim, *J. Power Sources*, 2024, **597**, 234116.
16 T. Krauskopf, H. Hartmann, W. G. Zeier and J. Janek, *ACS Appl. Mater. Interfaces*, 2019, **11**, 14463–14477.
17 P. Vadhva, J. Hu, M. J. Johnson, R. Stocker, M. Braglia, D. J. L. Brett and A. J. E. Rettie, *ChemElectroChem*, 2021, **8**, 1930–1947.
18 V. B. Mohan, K. Lau, D. Hui and D. Bhattacharyya, *Composites, Part B*, 2018, **142**, 200–220.